International Journal of Pharmaceutics 674 (2025) 125432

Contents lists available at ScienceDirect

International Journal of Pharmaceutics

journal homepage: www.elsevier.com/locate/ijpharm

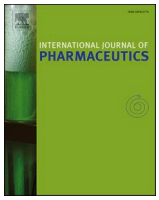

3D Printing with tuneable degradation: Thiol-ene and thiol-yne containing formulations for biomedical applications

A. Locks [a,b], B.J. Bowles [a], S. Brown [c], H.C. Hailes [b], S.T. Hilton [a,*]

[a] UCL School of Pharmacy, 29-39 Brunswick Square, London WC1N 1AX, United Kingdom
[b] UCL Department of Chemistry, University College London, Christopher Ingold Building, 20 Gordon Street, London WC1H 0AJ, United Kingdom
[c] Scott Bader, Wollaston, Wellingborough NN29 7RJ, United Kingdom

ARTICLE INFO

Keywords:
3D Printing
Digital Light Processing (DLP)
Thiol-Ene Polymers
Programmable Degradation
Biodegradable Materials
Biomedical Applications
Drug Delivery Systems

ABSTRACT

Despite advances in the range of materials that can be used in 3D printing and their applications across numerous scientific disciplines, the controlled breakdown of their solid structures after printing remains challenging. In this study we report the development of tuneable degradable 3D printed formulations, that could be 3D printed using standard digital light processing (DLP) and then degraded as required under mild conditions. Thirteen thiol-ene and thiol-yne formulations were designed to provide a range of tailored mechanical properties, with controlled degradation rates, and specific thermal behaviours with potential relevance to biomedical applications. The formulations ranged from ones with high stiffness for structural applications, through to those capable of rapid degradation. These formulations demonstrate full degradability and stability in physiological conditions, showing potential for future drug delivery applications pending further toxicity and release studies. This balance of degradability and mechanical robustness offers significant potential for enhancing patient safety and reducing the invasiveness of surgical treatments as directed by clinical needs.

1. Introduction

The global burden of chronic diseases continues to challenge both medical and scientific communities, necessitating a need for the continued development of new and effective therapeutic approaches to manage this high disease burden. Traditional treatments for internal conditions frequently include invasive surgeries and/or treatment via systemic therapy (Stephens and Aigner 2009). Whilst these approaches have shown efficacy, they are often accompanied by significant side effects, leading to the potential compromise of a patients' quality of life. The increased use of personalised medicine such as drug-releasing implants offers promising solutions to these problems (Krukiewicz and Zak 2016). These drug delivery implants function via the release of a high local concentration of therapeutic agents directly at or within the disease site, minimising systemic exposure and the associated adverse side effects that are often seen with traditional therapies (Wolinsky et al. 2012; Exner and Saidel 2008; Chew and Danti 2017).

Despite advances in drug eluting implants, the range of shapes needed for each patient intervention has hindered their utility via conventional manufacturing, due to the high costs associated with manufacture for a single patient. As such, 3D printing has become a key approach for investigations by biomedical scientists, due to its ability to

Abbreviations: 3D, Three Dimensional; ABS, Acrylonitrile Butadiene Styrene; API, Active Pharmaceutical Ingredient; Bis-GMA, Bisphenol A-glycidyl Methacrylate; BPO, Phenylbis(2,4,6-trimethylbenzoyl)phosphine Oxide; DBC, Dibutynyl Carbonate; dH_2O, Deionised Water; DiPETMP, Dipentaerythritol Hexakis(3-mercaptopropionate); DLP, Digital Light Processing; DSC, Differential Scanning Calorimetry; EDDET, 2,2′-(Ethylenedioxy)diethanethiol; FFF, Fused Filament Fabrication; GPC, Gel Permeation Chromatography; HDBC, 1,6-Hexanedibutynyl Carbonate; IBBC, Isobornylbutynyl Carbonate; IPDUB, Isophorone Diurethane Dibutyne; IPDUT, Isophorone Diurethane Hexakis(3-mercaptopriopionate); LED, Light-Emitting Diode; OB, Orasol Blue; PBS, Phosphate Buffered Saline; PEGDA, Polyethylene Glycol Diacrylate; PETMP, Pentaerythritol Tetrakis(3-mercaptopropionate); PG, Pyrogallol; PLA, Polylactide; PTMCPY-4MBA, Poly(trimethylene carbonate propynyl ester), 4-methylbenzyl alcohol initiated; PVA, Polyvinyl Acetate; S2, Sudan II; SE, Standard Error; SEM, Scanning Electron Microscopy; SLA, Stereolithography; SMP, Shape Memory Polymer; STL, Standard Tessellation Language; TCDDA, Tricyclodecane Dimethanol Diacrylate; TDMDBC, TDMol Dibutynyl Carbonate; TEMPIC, Tris[(3-mercaptopropionyloxy)-ethyl]-isocyanurate; T_c, Crystallisation Temperature; T_g, Glass Transition Temperature; T_m, Melting Temperature; TGA, Thermogravimetric Analysis; THF, Tetrahydrofuran; TMPTBC, Trimethylolpropane Tributynyl Carbonate; TPO, Diphenyl(2,4,6-trimethylbenzoyl)phosphine Oxide; UV, Ultraviolet.

* Corresponding author.
E-mail address: s.hilton@ucl.ac.uk (S.T. Hilton).

https://doi.org/10.1016/j.ijpharm.2025.125432
Received 18 November 2024; Received in revised form 2 March 2025; Accepted 3 March 2025
Available online 4 March 2025

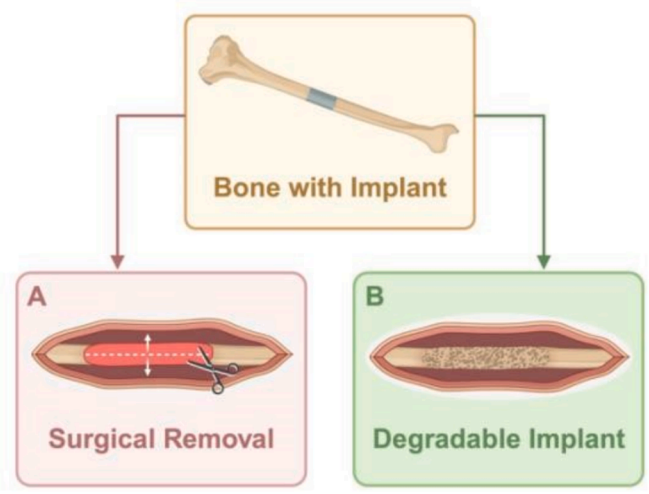

Fig. 1. Comparison of Implant Techniques. Panel A depicts a traditional metal implant requiring surgical removal. Panel B shows a fully degradable 3D-printed implant, illustrating its gradual degradation and the natural bone healing process, eliminating the need for surgical removal. Figure created with BioRender.com.

facilitate the fabrication of bespoke intricate structures that can't be made via conventional manufacturing (Liaw and Guvendiren 2019; Ligon et al. 2017). It therefore shows great potential for the creation of implants with precise drug release profiles and designs specifically tailored to the unique anatomy of individual patients (Palo et al. 2017; Goyanes et al. 2015).

3D printing has been employed in dentistry and orthodontic appliances (Liaw and Guvendiren 2017; Ligon et al. 2017), and in tissue engineering to produce functional tissues and organs (Liaw and Guvendiren 2017). 3D printing also offers precision in the creation of tissue scaffolds, ensuring biocompatibility, mechanical strength, and appropriate porosity (Leong et al. 2003; Yeong et al, 2004; Wang et al. 2023). 3D bioprinting has also successfully fabricated tissues such as skin, bone, and cardiac tissue (Liaw and Guvendiren 2017; Bulanova 2017), which can serve as platforms for drug testing and studying disease pathologies (Nyga et al. 2011).

The most commonly used 3D printing techniques are extrusion-based, such as fused filament fabrication (FFF) which constructs 3D structures by depositing successive layers of material that solidify upon cooling. Materials used with this technology typically include polylactide (Plastics Europe, 2022), polyvinyl acetate (PVA), and acrylonitrile butadiene styrene (ABS) (Palo, Holländer et al. 2017). However, a disadvantage of FFF is the need for high temperatures, (~200 °C) for processing, which can lead to the degradation of impregnated APIs. Whilst plasticisers can be added to decrease processing temperatures (Prasad and Smyth, 2015), FFF is limited in spatial resolution because the printhead's extrusion diameter is fixed and cannot be reduced beyond certain constraints (Palo et al. 2017; Norman et al., 2017). Stereolithography (SLA) is an alternative 3D printing technology that uses UV lasers to solidify liquid resin through photopolymerisation, offering high spatial resolution (Hutmacher et al. 2004; Ligon et al. 2017).

The use of SLA 3D printing in biomedical applications is however limited due to the restricted number of suitable commercial resins, but its precision still makes it an ideal approach for the production of surgical implants and drug delivery systems requiring intricate 3D structures. Its use of UV light for polymer formation makes it attractive as a technology as it does not necessarily expose thermolabile additives to the heat used in FFF printing (Palo et al. 2017). Most SLA resins use low molecular weight monomers, creating rigid materials, but with low flexibility (Hutmacher et al. 2004; Melchels et al. 2010). As such, scientists have explored a number of formulations designed to be used in SLA 3D printing, with (meth)acrylates (e.g. bisphenol A-glycidyl methacrylate (Bis-GMA)) or acrylic esters (e.g. polyethylene glycol diacrylate (PEGDA) (Revilla-León et al. 2019). These monomers are used due to fast printing times, stability over time and their customisable mechanical properties (Zhang and Xiao, 2018). However, the degradation of (meth)acrylate-based materials can lead to the formation of toxic by-products. These materials break down through ester linkage hydrolysis, producing poly(carboxylic acid)s and low molecular weight alcohols. While smaller molecules are typically excreted from the body, larger macromolecular acids tend to accumulate. This accumulation can cause persistent pH imbalances, preciptation of biomaterials, and subsequent irritation or toxicity (Heller et al. 2010; Husár et al. 2014; Ligon et al. 2017).

Vinyl esters, vinyl carbonates and vinyl carbamates present potential alternatives to (meth)acrylates that can undergo free radical polymerisation. These monomers are commonly used in biomedical applications such as soft contact lenses, but their use as photo-crosslinking agents remains relatively underexplored (Husar and Liska 2012). However, these materials still pose challenges as they are not fully degradable and their biocompatibility may be limited (Fig. 1). Implants that are not fully degradable can lead to complications such as chronic inflammation, infection, or necessitate surgical removal post-therapy (Wang et al. 2013).

To address these concerns, and building on our 3D printing formulations, we chose to investigate the potential of thiol-ene and thiol-yne systems as alternatives for creating fully degradable implants, with possible future applications in drug delivery. Thiol-ene and thiol-yne systems are notable for their robust polymer networks formed through step-growth photopolymerisation, which unlike radical polymerisation used in (meth)acrylates, is not inhibited by oxygen (Hoyle et al. 2004). Thiol-yne photopolymerisation also offers enhanced crosslinking density and uniform network formation compared to traditional UV-initiated systems (Wu et al. 2022). This ensures more consistent curing during the 3D printing process, enhancing the structural integrity of the fabricated implants. Additionally, these systems can be engineered to degrade at controlled rates, overcoming the challenges posed by permanent implants. The thiol-ene reactions typically result in polymers that degrade into smaller by-products, which prior studies suggest are non-toxic and can be assimilated or excreted by the body (Balakrishnan and Jayakrishnan 2005; Gao et al. 2002; Melchels et al. 2010). Thus, thiol-ene and thiol-yne based implants offer a promising approach for developing biodegradable materials with potential for future use in drug delivery systems, pending additional studies (Jain 2000; von Burkersroda et al. 2002). This research builds upon existing knowledge while proposing these materials as potential alternatives due to their adaptability and controlled degradation profiles.

2. Materials and methods

2.1. Resin reagents

1,7-Octadiyne was purchased from Acros Organics (Antwerp, Belgium). 2,2′(Ethylenedioxy)diethanethiol (EDDET) was purchased from Merck (Massachusetts, United States). Pentaerythritol tetrakis(3-mercaptopropionate) (PETMP) was purchased from Merck (Massachusetts, United States). Dipentaerythritol hexakis(3mercapropriopionate) (DiPETMP) was purchased from Tokyo Chemical Industry (Tokyo, Japan). Phenylbis(2,4,6-trimethylbenzoyl)phosphine oxide (BPO) was purchased from Arkema (Colombes, France). Pyrogallol (PG) was purchased from Acros Organics (Antwerp, Belgium). Sudan II (S2) was purchased from Acros Organics (Antwerp, Belgium). Orasol Blue (OB) was purchased from Sun Chemicals (New Jersey, United States). The remaining constituents of formulations BB01-13 were synthesised according to the methods in S1.4. Clear UV resin was purchased from 3D Prima (Malmö, Sweden).

Table 1
Theoretical and expected/target structural data (molecular formula and molecular weight in g/mol) of synthesised compounds that make up components of the 3D printed formulations. Structures of the abbreviated synthesised compounds, in addition to commercially available reagents in the formulations are shown in Figs. 6 and 7.

Name of compound	Theoretical			Expected/targeted	
	Molecular formula	Molecular weight (g/mol)	Repeat unit values	Molecular formula	Molecular weight (g/mol)
$(PTMCPY)_n$, **1**	$C_{(8+9n)}H_{(10+12n)}O_{(1+5n)}$	$122.07 + 198.05n$	n = 4	$C_{44}H_{50}O_{21}$	914.27
DBC, **2**	$C_9H_{10}O_3$	166.06			
HDBC, **3**	$C_{16}H_{22}O_6$	310.14			
IBBC, **4**	$C_{15}H_{22}O_3$	250.16			
TDMDBC, **5**	$C_{22}H_{28}O_6$	388.19			
TMPTBC, **6**	$C_{21}H_{26}O_9$	422.16			
IPDUB, **7**	$C_{20}H_{30}N_2O_4$	362.22			
IPDUT, **8**	$C_{(17+29n)}H_{(27+47n)}O_{(8+10n)}S_{(4+4n)}N_{(2n)}$	$487.06 + 711.21n$	n = 1	$C_{46}H_{74}N_2O_{18}S_8$	1198.27
TEMPIC, **9**	$C_{18}H_{27}N_3O_9S_3$	525.09			

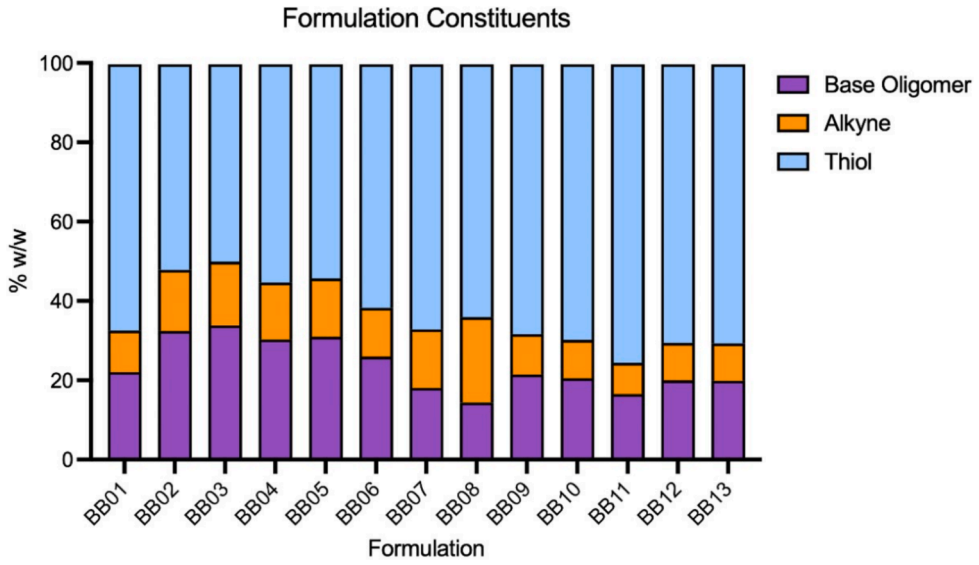

Fig. 2. Composition of formulations BB01-13 as the percentage by weight (% w/w) of each constituent in the 13 formulations. Note: The percentages of the photoinitiator and dye are too small to be visually represented on this graph. Detailed constituent names and precise percentages (% w/w) are provided in Fig. S1.

2.2. Formulation constituents for mould-curing and 3D printing

A summary of the theoretical and expected structural data for the synthesised compounds of the formulations is provided in Table 1, highlighting the molecular weights and targeted repeat unit values where applicable. Fig. 2 illustrates the composition of formulations BB01-13, detailing the relative percentages by weight of the base oligomer, poly(trimethylene carbonate propynyl ester), (PTMCPY, compound **1**) alkyne (compounds **2**–**7**) and thiols (compounds **8, 9**). The remaining alkyne and thiol components were commercially obtained, with their structures shown in Fig. 6 and Fig. 7, alongside the structures of the synthesied compounds. Additional formulation components, such as the photoiniator and photoabsorber, are provided in Figs. S2-S4.

2.3. Preparation of mould-cured and 3D printed formulations

A 25 mL round bottom flask was preheated at 50 °C on a heating block. PTMCPY, IPDUB, and TEMPIC, were melted via direct heating at 100 °C, 100 °C, and 80 °C, respectively. A sequential gravimetric addition method was used for each formulation. The photoinitiator e.g. BPO, PG and photoabsorber e.g. S2 were weighed first, with zeroing of the balance between each addition. A tolerance range of ± 0.5 mg was deemed acceptable for this protocol. The alkyne components were incorporated using the same process. The formulation was stirred under nitrogen followed by gentle reheating until a homogeneous mixture was achieved. The thiol components were subsequently added under ambient conditions, after which the mixture was returned to the heating block under nitrogen atmosphere and stirred until homogeneous. The final mixture was allowed to cool to room temperature under a

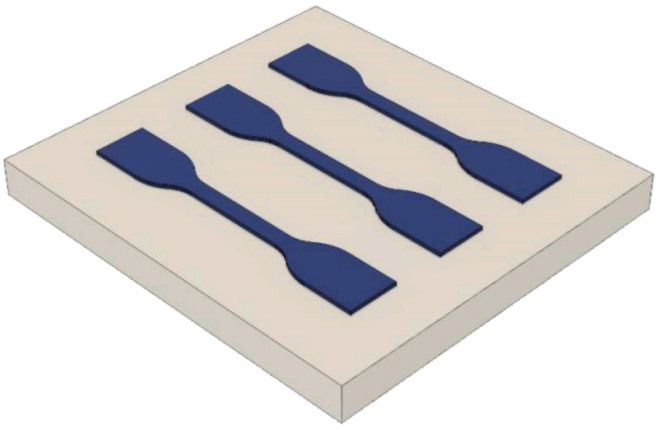

Fig. 3. Visualisation of the silicone moulds filled with photoreactive resin. Each mould contains three wells, depicted here fully loaded with resin for the curing process.

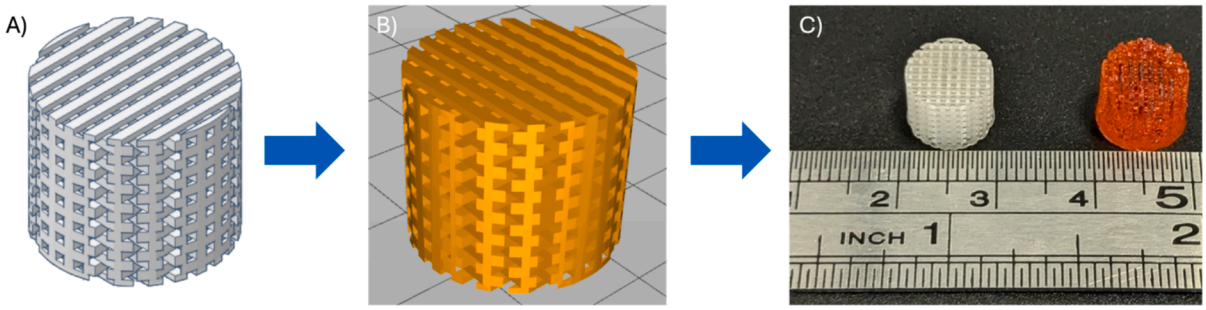

Fig. 4. a) Tinkercad generated design showing a 3D cylindrical lattice with 1 mm pore size, b) visualised in Asiga Composer software before being printed using an Asiga DLP 3D printer with 9.07 x 9.08 x 7.51 dimensions, c) final prints indicate clear resin and BB10 3D cylindrical lattice with 1 mm pore size, measured in cm.

protective aluminium cover to prevent photo reactivity prior to mould curing/3D printing.

2.4. Mould-cured formulations

Upon cooling, the synthesised photoreactive resin was prepared for casting. Silicone moulds designed for ISO 527–2 Type 5A specimens, typically used for tensile testing but also used in this work for degradation, swelling studies, and thermal analysis, were placed on the curing platform of a Form Cure (Formlabs. Somerville, Massachusetts, USA). The resin was dispensed via pipette into the moulds, ensuring that no air bubbles were trapped during the process. Each silicone mould contained three wells for specimen casting (Fig. 3), with a total of two moulds available, allowing the production of up to six specimens per resin batch.

The filled moulds were subjected to an initial cure of 15 min without heat in the Form Cure curing oven. Subsequently, the specimens were extracted from the moulds and subjected to a second curing phase of 15 min without heat to ensure the stabilisation of the mechanical properties. Post-cure cleaning involved the use of acetone-soaked wipes to remove any uncured resin from the specimen surfaces. A final curing phase was executed for a period of 10 h at 60 °C.

2.5. 3D printed formulations

The 13 formulations, in addition to an acrylate-based Clear UV resin for comparison, were 3D printed using the digital light processing technique and an Asiga MAX X27 printer (Asiga, NSW, Australia), with pixel resolution: 27 μm; layer height: 100 μm; light power: 6.62 mW/cm^2.

The 3D printed formulations differed slightly from the mould-cured formulations, due to the presence of S2 instead of OB at the same % w/w.

A cylindrical lattice structure with 1 mm pore size was generated for degradation testing purposes using Tinkercad software (Fig. 4) and exported as an STL file. The structure had x, y, and z dimensions of 9.07, 9.08 and 7.51 mm. The 3D printing was controlled with Asiga Composer software (Asiga, V2.0.4, NSW, Australia), which adapted the method based on input data from preliminary z-curing of the formulations. Additional 3D printing parameters are detailed in Table S1, and the Jacobs Working Curve for formulation BB10 it provided in Fig. S5.

Following printing, the constructs were washed with isopropyl alcohol in order to remove unpolymerised resin. A final curing cycle was then performed using the Form Cure box (Formlabs. Somerville, Massachusetts, USA) for 10 min at 60 °C to complete the polymerisation of the samples.

2.6. Tensile testing

Tensile testing was carried out to determine the mechanical properties of the materials. Testing was conducted using a Shimadzu EZ-LX Test Compact Table-Top Universal Tester equipped with a 5 kN EZ-Test-X load cell. The system utilised upper and lower tensile joints, along with 5 kN manual wedge grips featuring file teeth grip faces designed for flat specimens. Samples were initially secured in the lower grip, and the upper grip was then adjusted to securely hold the upper shoulder of the sample, ensuring a consistent gauge length of 28 mm. Shimadzu Trapezium X software was used to configure, execute, and analyse the tests.

To ensure precision, a zero-force hold function was applied during loading to prevent errors. The testing mode was set to single, with the test type specified as tensile. A pretest force of 0.2 N was applied, and the test speed was maintained at 10 mm/min, which provided a balance between accuracy and efficiency for the range of materials studied. Testing continued until sample failure was detected, with stress–strain curves generated in real time during the process. Post-test data included maximum force (N), maximum stress (tensile strength, MPa), elongation at break (mm), and energy (J), with additional parameters such as elongation at break (%), (tensile) toughness (kJ/m^3), and Young's modulus (MPa) calculated manually. All reported values were within 1 standard error (SE). Each resin formulation was tested in triplicate.

2.7. Degradation studies

For degradation tests in 1 M NaOH, samples BB01 to BB13 in addition to cylindrical lattice structures with 1 mm pore size were weighed and their dimensions were measured using Vernier callipers. Each sample was placed in an individual glass vial and 10 mL of 1 M NaOH solution was added to each vial. The vials were occasionally agitated and visibly inspected at specified intervals: 30 min, 1 h, 2 h, 4 h, 8 h, 1 d, up to 7 d. During each observation, the degradation state was categorised as: no degradation, partial degradation, significant degradation, or complete degradation. Supporting images were captured for each degradation state (Figs. S6-S7).

In assessing degradation in Phosphate Buffered Saline (PBS) pH 7.4, as with the NaOH test, samples BB01 to BB13 were weighed and their dimensions measured using Vernier callipers. Each sample was placed in a separate glass vial, followed by the addition of 10 mL of PBS (pH 7.4). The vials were occasionally agitated and inspected at intervals of 1 d, 3 d, 7 d, 13 d, and 31 d. The degradation observations and documentation process were analogous to the NaOH test. Supporting images were captured for each degradation state (Figs. S8-S9).

It's important to note that the dye utilised in the formulations is insoluble in water. Therefore, any particulate remnants in the vial post-degradation can be attributed to the undissolved Orasol Blue or Sudan II dye, indicating complete sample degradation.

2.8. Swelling studies

For swelling studies in deionised water, triplicate samples (BB01 to BB13) were weighed, and their dimensions were recorded using Vernier callipers. For each formulation, three samples were placed in individual glass vials, and 10 mL of distilled water was added. At predetermined

intervals (0.5 d, 1 d, 3 d, 5 d, 7 d, and 32 d), samples were lightly blotted to remove excess water using a paper towel and then weighed. Dimensions were also measured using the Vernier callipers during each interval.

2.9. Scanning electron microscopy imaging

SEM images were acquired using a Phenom ProX SEM (Thermo Fisher Scientific). This desktop SEM model provides high-resolution imaging and was selected for its ability to effectively illustrate the microstructural changes in the studied samples.

Prior to imaging, samples were attached to an adhesive carbon tab that was stuck on a brass stub. The samples were sputter-coated with a thin layer of gold to increase their conductivity, minimising sample charging under the electron beam.

All samples were imaged under high vacuum conditions. An electron beam with an acceleration voltage of 5 kV was employed. Images were taken using the electron detector to capture the sample's topography at 275x magnification. To track changes over time, images were taken at two distinct intervals: immediately after sample preparation, and after 2 months of immersion in PBS pH 7.4 solution at 37 °C. Surface features such as cracks, erosions, and other degradation patterns were assessed. The observed morphological changes were correlated with the sample formulations and degradation rates.

2.10. Thermogravimetric analysis

Thermogravimetric Analysis (TGA) was used to elucidate the degradation temperature of the 3D printed materials. TGA analysis was conducted using a TA Discovery TGA instrument (TA Instruments, USA) under a nitrogen atmosphere with a flow rate of 25 mL/min. The samples were heated in aluminium pans from ambient temperature to 600 °C at a constant rate of 10 °C/min.

2.11. Differential scanning calorimetry

Differential Scanning Calorimetry (DSC) analysis was used to elucidate the glass transition temperature (T_g) of the photocured materials, to determine the temperature at which the polymers could exhibit shape memory properties. DSC was carried out using a Multi-Sample X3 DSC system (TA Instruments, USA), calibrated with indium (melting temperature, T_m = 156.6 °C; enthalphy of fusion, ΔH_f = 28.71 J/g). The measurements were conducted under a nitrogen atmosphere, with a base purge rate of 300 mL/min and a cell purge rate of 50 mL/min. Approx. 5 mg of each of the 13 formulations was loaded into a T_{zero} aluminium pan and crimped with T_{zero} lid. Three different heating methods were employed: a standard heating ramp at 10 °C/min from −80 °C to 200 °C; a standard heating ramp at 100 °C/min from −80 °C to 200 °C; a heat-cool-heat cycle where the samples were ramped 10 °C/min from −80 °C to 200 °C, down to −80 °C at 10 °C/min and back up to 200 °C at 10 °C/min. Trios software (TA Instruments, USA) was used to analyse the T_g in all heating methods.

2.12. Gel permeation chromatography

Gel permeation chromatography (GPC) was used to determine the polydispersity of the base oligomer, PTMCPY, and the thiol IPDUT. The analysis was conducted using a GPC system equipped with a Viscotek GPC max chromatograph, a Waters 410 differential refractive index detector, and a Gilson 831 column oven. Samples were prepared by dissolving approximately 3 mg of material per mL of tetrahydrofuran (THF), with 2 μL/mL toluene added as a flow marker. The setup included two Polymer Labs PLgel Mixed E columns (3 μm, 300 x 7 mm) maintained at 40 °C. The mobile phase consisted of 100 % THF (Fisher Scientific GPG grade) at a flow rate of 1 mL/min, and an injection volume of 100 μL was used for each sample.

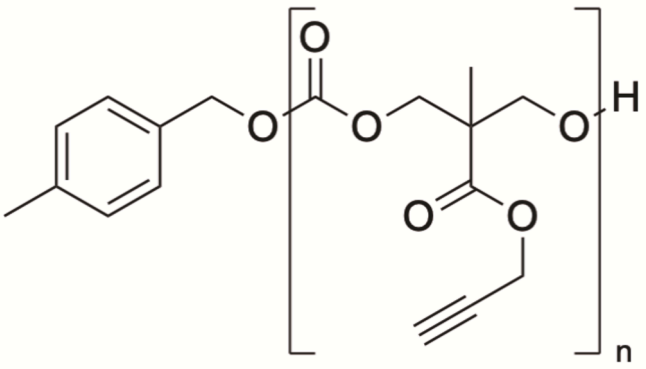

Fig. 5. Structure of the base oligomer PTMCPY, **1**.

3. Results and Discussion

The development of the 13 formulations used for mould-curing and 3D printing in this study aimed to understand how variations in the chemical structure and ratio of thiol and alkyne compounds affect the physical properties of the resulting photopolymers, particularly focusing on their mechanical strength, degradation rates and printability (Esfandiari, Ligon et al. 2013; Oesterreicher, Gorsche et al. 2016; Oesterreicher, Ayalur-Karunakaran et al. 2016; Oesterreicher et al., 2017).

Poly(trimethylene carbonate propynyl ester), (PTMCPY) was chosen as the base oligomer (Fig. 5) across all formulations due to its biodegradability and compatibility with medical applications (Wu, Simpson et al. 2021). This component formed the backbone of each polymer network, ensuring the final printed objects can degrade safely within biological environments without causing adverse effects.

The rationale for the synthesised alkyne components of the formulations was as follows: Dibutynyl carbonate (DBC), **2** was used due to it containing a hydrolytically sensitive carbonate group which may aid the degradation rate and reduce the size of degradation fragments (Oesterreicher et al., 2016); 1,6-Hexanedibutynyl carbonate (HDBC), **3**, was included based on literature precedence where it is used as a reactive diluent in acrylate and methacrylate-based 3D printing formulations; Isobornylbutynyl carbonate (IBBC), **4**, similar to isobornyl acrylate and isobornyl methacrylate, was used to increase flexibility and hardness as its monofunctional nature is expected to impart more flexible properties, and its high T_g should impart hardness; TDMol dibutynyl carbonate (TDMDBC), **5**, was synthesised as an equivalent of tricyclodecane dimethanol diacrylate (TCDDA) (renowned for its low shrinkage index via reduction of internal stresses (Albelasy et al., 2024; Revilla-León et al., 2019). Therefore TDMDBC's constrained cyclic aliphatic backbone could provide stiffness and a higher T_g, indicating increased rigidity; Trimethylolpropane tributynyl carbonate (TMPTBC), **6**, similar to trimethylolpropane triacrylate and trimethylolpropane trimethacrylate, was used for rigidity and strength by increasing crosslinking density, due to its trifunctional nature; Isophorone diurethane dibutyne (IPDUB), **7**, a urethane-based oligomer, was selected to improve the mechanical properties, introducing toughness via hydrogen bonding which can diminish crack-propagating forces (Huang et al. 2014), though its use may require balancing with other low viscosity constituents to manage overall formulation viscosity (Tan et al. 2021); 1,7-Octadiyne, **10**, a difunctional alkyne was used primarily to reduce the viscosity of formulations. The structures of all synthesised alkyne components are summarised in Fig. 6.

For the synthesised thiol components, isophorone diurethane hexakis(3-mercaptopriopionate) (IPDUT), **8**, and tris[(3-mercaptopropionyloxy)-ethyl]isocyanurate (TEMPIC), **9**, were both utilised to increase the toughness of the formulations in the same manner as explained with IPDUB, **7** (Naira et al. 2010; Olofsson et al., 2016). Pentaerythritol tetrakis(3-mercaptopropionate (PETMP), **11**, a

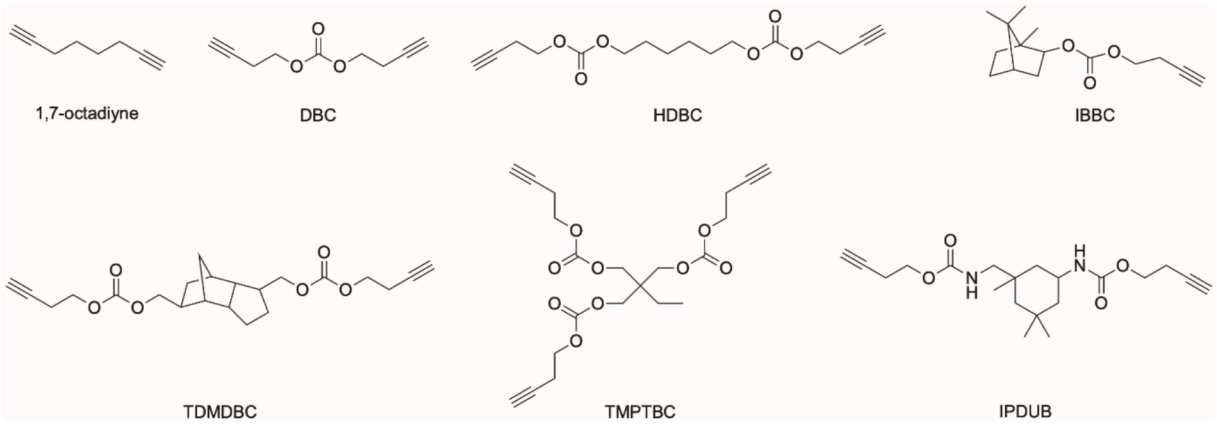

Fig. 6. Structures of alkyne components: DBC, **2** HDBC, **3**, IBBC, **4**, TDMDBC, **5**, TMPTBC, **6**, IPDUB, **7**, and 1,7-octadiyne, **10**.

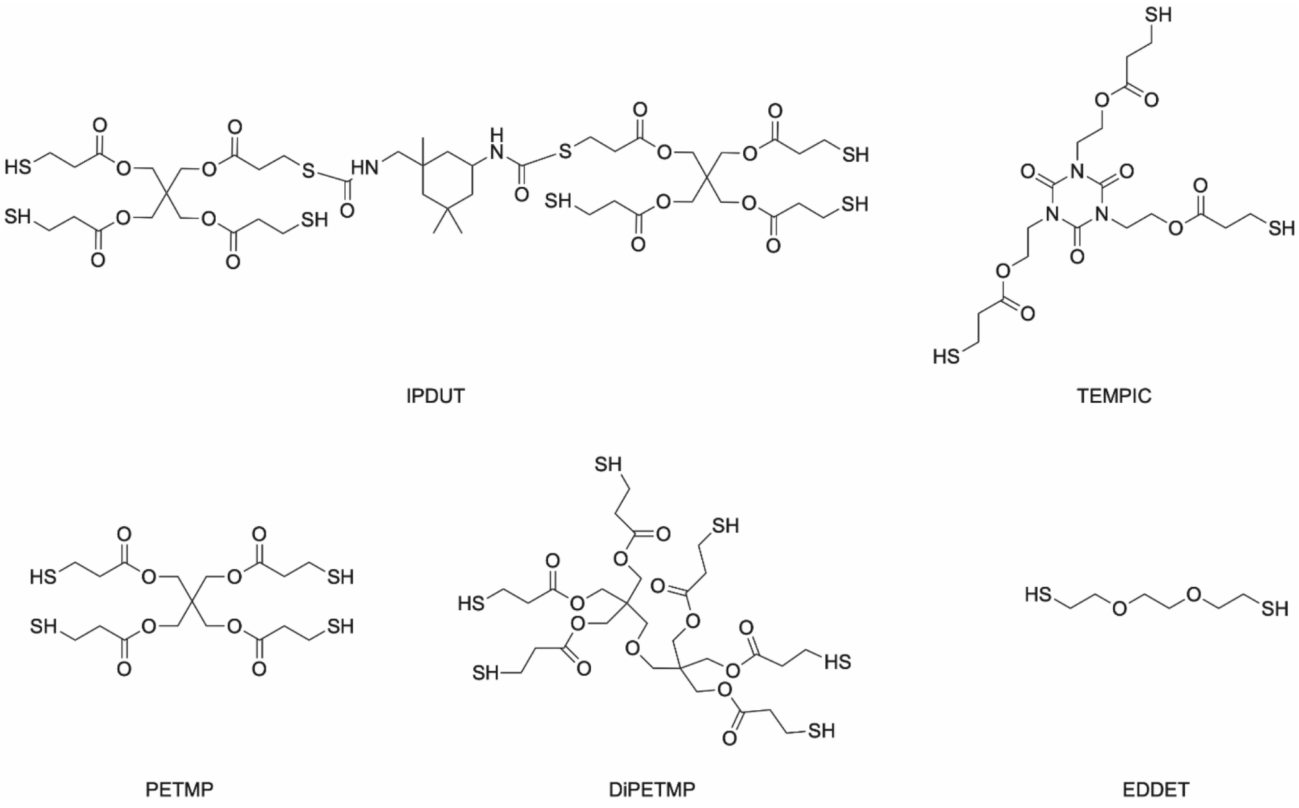

Fig. 7. Structures of thiol components: IPDUT, **8** TEMPIC, **9** PETMP, **11**, DiPETMP, **12**, EDDET, **13**.

tetrafunctional thiol, was used to aid in enhancing the crosslinking density and mechanical integrity (Oesterreicher et al. 2016), dipentaerythritol hexakis(3-mercapropriopionate (DiPETMP), **12**, to increase thiol functionality, contributing to greater stiffness and toughness (Oesterreicher et al. 2016). Finally, 2,2′-(ethylenedioxy)diethanethiol (EDDET), **13**, a difunctional thiol with ether groups, was utilised as it has a low viscosity therefore reduces crosslinking density and increases the backbone flexibility of the polymer networks, influencing the softness and adaptability of the materials. The structures of all synthesised thiol components are summarised in Fig. 7. Structures of the photoinitiators (BPO, PG) and photoabsorber (S2) used in these formulations are provided in Figs. S2-S4.

Regarding the photoinitators, phenylbis(2,4,6-trimethylbenzoyl) phosphine oxide (BPO) was chosen since it requires only a small quantity to achieve a quick cure, due to the fact that it creates two radicals as opposed to other common phosphine oxides such as diphenyl(2,4,6trimethylbenzoyl)phosphine oxide (TPO). Pyrogallol (PG) was also used as it prevents curing in non-irradiated areas and prevents premature gelation upon storage of resins, ensuring accuracy and stability of the printed structures. It is specifically used as a photoinitiator in thiolyne formulations (Esfandiari et al. 2013). Orasol Blue (OB) was also used as a dye for visual tracking and quality control during the printing process, ensuring consistency and uniformity in the fabrication of test specimens.

In the initial formulation series (BB01 to BB06), Fig. 2**,** Fig. S1, the stoichiometric ratios of alkynes to thiols were consistently maintained at two thiol to one alkyne to ensure maximum alkyne/thiol group conversion and achieve maximum crosslinking density. Each alkyne group ideally reacts with two thiol groups to form a stable dithioether linkage, so this 2:1 ratio is important for optimal polymerisation kinetics, mechanical properties and material stability (Wu et al. 2021). Since the

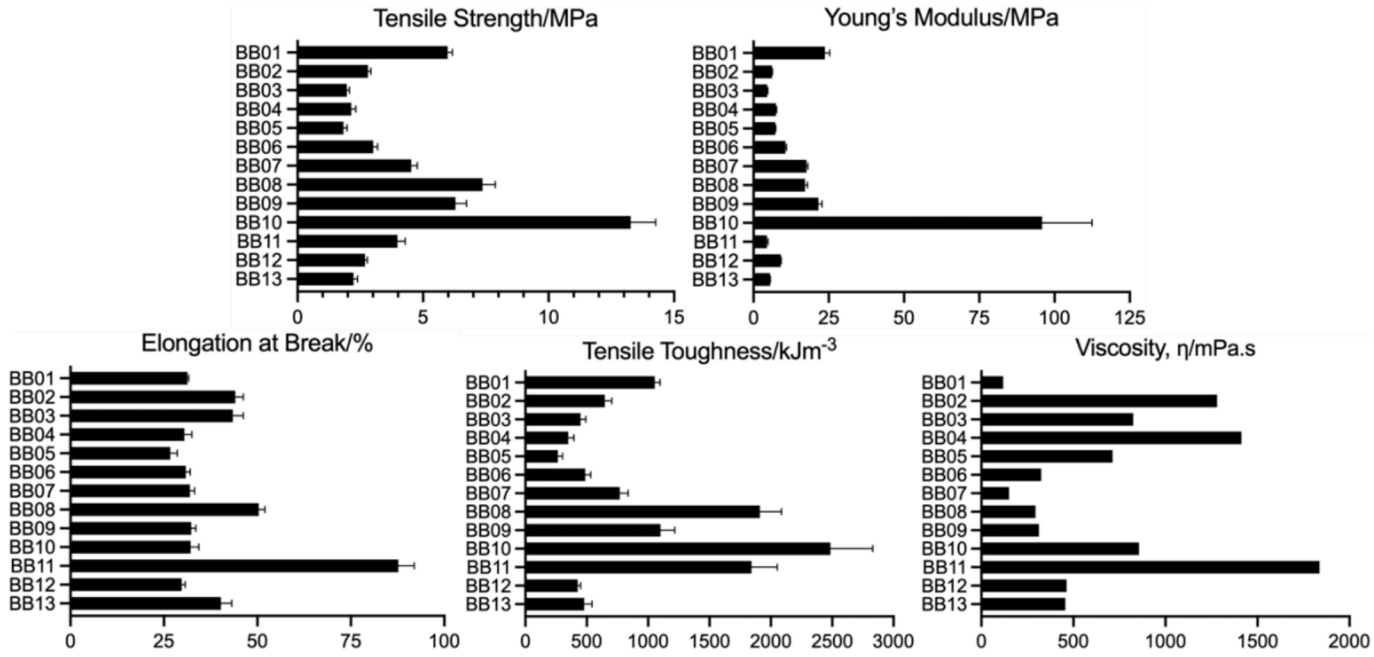

Fig. 8. Mechanical and rheological properties of the 3D printed formulations. Mechanical properties consist of tensile strength (MPa), Young's modulus (MPa), elongation at break (%) and tensile toughness (kJ/m^3). Standard error is present for all samples. Rheological properties displaying the viscosity at specified temperatures are provided for each sample. Data represents the mean values for each sample. Detailed values for each formulation are provided in Table S2.

ratios were maintained, this meant that the influence of substituting the noncarbonate alkyne components on the material properties could be investigated. The rationale was developed based on literature precendence demonstrating how altering stoichiometric ratios in thiol-yne formulations enables selective functionalisation of 3D printed objects (Roppolo et al. 2019). BB07 and BB08 formulations were prepared with altered stoichiometric ratios of IPDUB to evaluate their impact on viscosity and subsequent material characteristics. The series from BB09 to BB13 contained variations in the thiol components to further understand their effect on the resultant mechanical properties.

The study also focused on viscosity considerations, where 2000 mPa.s was considered the maximum viscosity for room temperature 3D printing, with a viscosity below 1000 mPa.s indicating in general that the material is easier to 3D print at room temperature.

The materials were then analysed by GPC to reveal insights on polymer uniformity, tensile testing to assess how varying the components and ratios of the formulations affected mechanical properties, and degradation studies to study if the formulations were fully degradable and if tuneable degradation could be achieved by varying each formulation. Swelling studies were carried out to assess water uptake, and TGA/DSC to evaluate thermal properties.

3.1. *Analysis of the mould-cured formulations*

The Gel Permeation Chromatography (GPC) results for IPDUT showed main peaks at M_n 3908 gmol^{-1}, M_w 5196 gmol^{-1}, while for PTMCPY, the main peaks were at M_n 1316 gmol^{-1} and M_w 1899 gmol^{-1}. As shown in Table 1, the targeted number of repeat units for PTMCPY was four, with a theroetical M_w of 914.27 gmol^{-1}. However, the actual M_w was 1899 gmol^{-1}, indicating that the average number of repeat units was approximately eight. For IPDUT, the target number of repeat units was one, with a theoretical M_w of 1198.27 gmol^{-1}. The actual M_w was 5196 gmol^{-1}, suggesting an average of four or five repeat units. Although the targeted repeat units were not achieved, the GPC results revealed a consistent molecular weight across the samples and hence suggested a uniform polymer network (Fig. S10). It is important to note that the GPC was calibrated using polystyrene standards and a general method used rather than one optimised for the specific oligomer tested; therefore, the M_n should not be regarded with as much accuracy as the M_w value.

Tensile testing was carried out on BB01-13 to determine how varying the components and ratios of the formulations affected mechanical properties. The hypotheses for the formulations with regards to tensile testing were as follows: 1) an increase in the alkyne functionality and therefore crosslinking density should increase rigidity of the materials; 2) an increase in the thiol functionality and therefore crosslinking density should increase the rigidity of the materials; 3) more thioether bonds will introduce more softness but not more flexibility; 4) the introduction of more carbonate ester groups should decrease toughness (Kim et al. 2021); 5) the introduction of more urethane groups should increase toughness. The tensile testing values are summarised in Fig. 8.

In the series BB01 to BB06, where the w/w ratio of alkynes to thiols were consistent, varied mechanical responses were observed due to the substitution of different non-carbonate alkyne components. Contrary to hypothesis 1, which suggested that increased alkyne functionality and therefore crosslinking density should increase material rigidity, the actual results demonstrated a deterioration in toughness, particularly with the use of 1,7-octadiyne. The tensile strength varied from 1.83 MPa (BB05) to 5.98 MPa (BB01), with corresponding tensile toughness ranging from 265 kJ/m^3 (BB05) to 1050 kJ/m^3 (BB01). This unexpected outcome suggests that the lower molecular weight and higher alkyne group content per gram in formulations like BB02 (Fig. 2) contributed to increased crosslink density and resultant rigidity.

BB09 to BB13 formulations contained variations in the thiol components and demonstrated that changes in thiol functionality affect the mechanical properties, supporting hypothesis 2. For example, BB10, which contains DiPETMP, **12**, had the highest tensile strength (13.3 MPa) and Young's modulus (95.9 MPa) within this group of formulations, supporting the hypothesis that increased thiol functionality enhances crosslink density, thereby increasing stiffness and toughness. However, the elongation at break did not significantly change with variations in thiol components e.g. BB12 contained 42 % IPDUT, 28 % EDDET with 30 % elongation at break, BB13 contained 70 % PETMP with 40 % elongation at break, suggesting that increased crosslink density contributes to stiffness but does not necessarily enhance flexibility as stated in hypothesis 3.

When comparing formulations such as BB06 (includes DBC, **2**) to BB05 (includes HDBC, **3**), it demonstrated the impact of carbonate ester groups on the mechanical properties, addressing hypothesis 4. BB06 has a tensile strength of 3.01 MPa and an elongation at break of 30.8 %, which is higher than BB05 with a tensile strength of 1.83 MPa and elongation at break of 26.7 %. This indicates that despite the carbonate ester groups not drastically enhancing strength, they provided better elongation, therefore creating a balance between rigidity and ductility. These properties might be beneficial for applications requiring flexibility but contradict the hypothesis that more carbonate ester groups should decrease toughness.

Since BB08 incorporated a higher *w/w* ratio of IPDUB, **7** (14.4 %) in comparison to BB07 (4.93 %), it was observed that BB08 showed significant increases in tensile toughness (1910 kJ/m^3, in comparison to 769 kJ/m^3 for BB07) and elongation at break (50.4 % for BB08, in comparison to 32.0 % for BB07), confirming hypothesis 5. These results suggest IPDUB as a promising alkyne component, offering satisfactory viscosities of 294 mPa.s and 313 mPa.s for BB07 and BB08 respectively, with printing viscosities noted to be ideal below 1000 mPas.

BB11′s results highlighted that TEMPIC, **9**, marginally impacts mechanical properties, since it contained 75.3 % TEMPIC and a viscosity of 1840 mPa.s, whereas the remaining formulations ranged from 120 to 1410 mPa.s. BB10 emerged as a superior formulation with robust tensile strength, Young's modulus, and toughness, alongside an optimal printing viscosity, making it more suitable for high-stiffness applications such as bone or cartilage analogs. Although BB11 displayed the highest elongation at break and considerable toughness, it had suboptimal printing viscosity, indicating the need for optimisation to enhance its application potential for flexible or soft tissue mimetic applications. In this instance, heating techniques such as hot lithography could be used as an alternative approach to achieve suitable printing viscosities (Pezzana et al. 2022).

Overall, the tensile testing results revealed that the mechanical properties of the formulations are sensitive to both the type and functionality of the thiol and alkyne components, as well as the incorporation of carbonate ester groups. These findings demonstrate the importance of balancing crosslink density, molecular weight, and functional group substitution to optimise the material properties such as flexibility, rigidity, or toughness for biomedical and structural applications.

3.2. 3D Printed formulations

Since the PTMCPY based resins showed excellent performances regarding curing rate and conversion together and their networks provide decent mechanical properties from the tensile testing, the formulations were chosen for the evaluation for its 3D printability, offering the advantage of low material consumption, short production times and sufficiently high resolution. The Asiga DLP printer uses a 385 nm LED as its light source. Sudan II (S2) was chosen as a photoabsorber because it absorbs light in same wavelength as the light source, hence it permits control over cure depth (and hence Z dimension printing accuracy) and also prevents premature gelation/polymerisation upon storage of resins.

The commercially available acrylate-based Clear UV resin and BB10 were successfully printed for degradation studies, generating printlets with dimensions closely matching the input CAD mesaurements (Fig. 4) due to the high resolution (27 μm) of the Asiga printer. For both resins, the targeted dimensions were 9.07, 9.08 and 7.51 mm, with achieved dimensions of 9.96, 9.12 and 7.54 mm. For BB10, the achieved dimensions were 9.96, 9.12, and 8.19 mm. The slight deviations were attributed to overcuring caused by additional supports required for successful printing, reflecting the challenges in achieving perfect CAD fidelity.

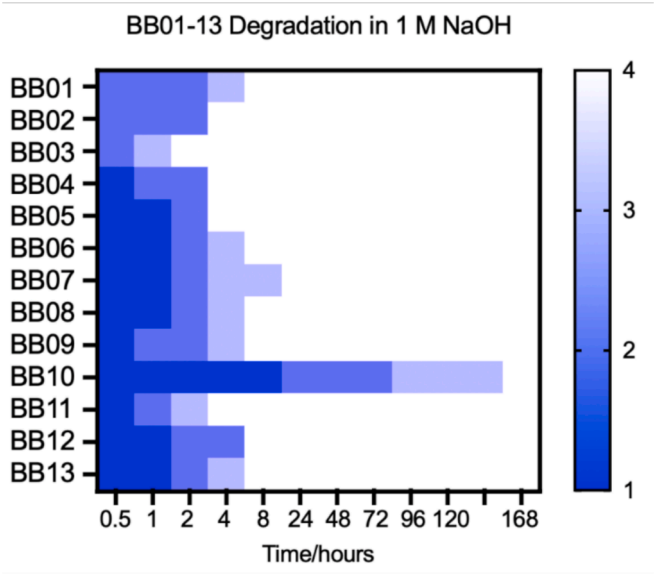

Fig. 9. Heatmap representing BB01-13 degradation in 1 M NaOH over 7 days. Each cell represents the degradation state of a sample at a specific time interval, with colour intensity indicating the extent of degradation: 1 (no degradation); 2 (partial degradation); 3 (significant degradation); 4 (complete degradation).

3.3. Degradation studies

The hypotheses for the formulations with regards to degradation studies were that an increase in the alkyne functionality and therefore crosslinking density should reduce degradability, an increase in the thiol functionality and therefore crosslinking density should reduce degradability, the introduction of more carbonate ester groups should increase degradability, and the introduction of more urethane groups should decrease degradability.

Degradation studies were conducted in 1 M sodium hydroxide (NaOH) and phosphate buffered saline (PBS) pH 7.4. These studies involved all 13 mould-cured formulations, with a focus on assessing the rate and extent of material breakdown under these conditions.

3.3.1. Degradation in sodium hydroxide solution

The mould-cured formulations exhibited a wide range of degradation times in 1 M NaOH (Fig. 9), with BB03 exhibiting the fastest complete degradation after 24 h, whereas BB10 exhibited the slowest complete degradation after 7 d (Fig. 10). It is important to note that the use of 1 M NaOH in this study represents an accelerated degradation test designed to assess chemical stability and degradation mechanisms under extreme basic conditions. This approach allows for direct comparisons to existing commercially used acrylate formulations, evaluating whether the tested materials demonstrate distinct degradation behaviour under extreme basic conditions.

The 3D-printed BB10 formulation showed significantly faster degradation in 1 M NaOH when printed as a cylindrical lattice structure with a 1 mm pore size (Fig. 11), compared to its equivalent mould-cured formulation. This accelerated degradation can be attributed to the increased surface area of the lattice structure. Among all the formulations, BB10 was the most durable, yet it still demonstrated a higher rate of full degradation compared to a commercially available acrylate resin, which are used in biomedical applications. By 6 h, BB10 was mostly depolymerised, and complete depolymerisation was achieved by 10 h. The fact that BB10 showed the most superior tensile strength, Young's modulus, and toughness and yet is fully degradable further demonstrates the potential of this material for possible implants that need to withstand the physiological environment while providing targeted therapeutic action without the need for surgical removal after treatment.

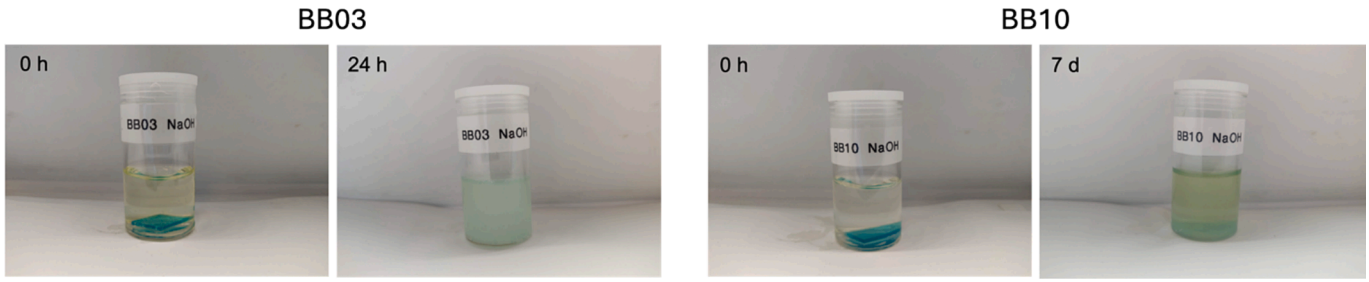

Fig. 10. Degradation photos of BB03 and BB10 mould-cured formulations in 1 M NaOH at 0 h and complete degradation at 24 h (BB03) and 7 d (BB10).

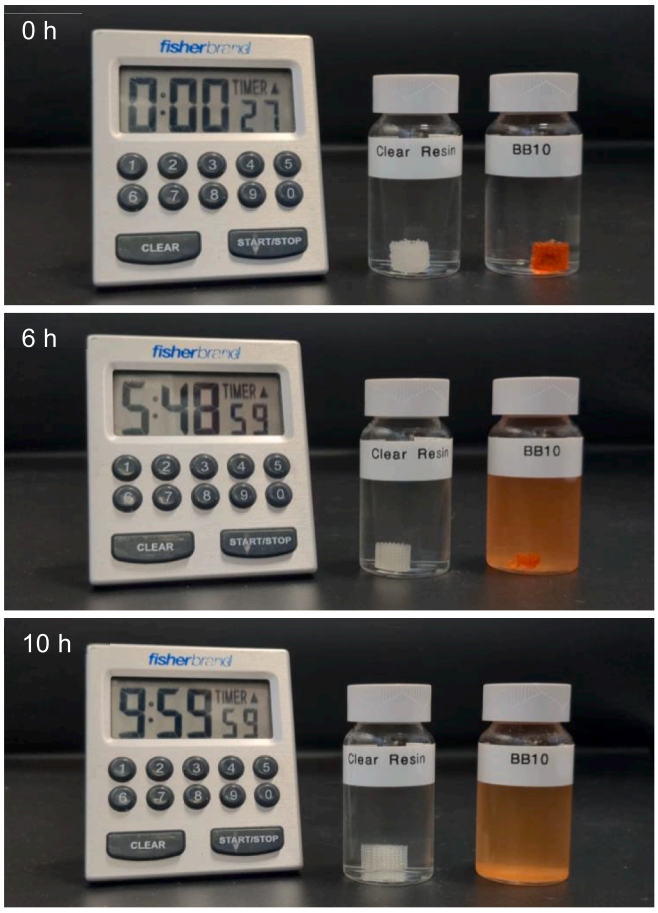

Fig. 11. Clear Resin and BB10 3D cylindrical lattices with 1 mm pore size printed using an Asiga DLP 3D printer in 1 M NaOH at 0 h (no degradation), 6 h (significant degradation) and 10 h (complete degradation).

Given the chemical structures and components in the formulations, several factors may have influenced the differing rates of degradation when exposed to 1 M NaOH.

BB02 and BB08 both include TDMDBC, **5** and IPDUB, **7** respectively, both of which have a high alkyne functionality. The degradation data shows that BB02 and BB08 have a delayed onset of degradation until 4 h, suggesting increased resistance to degradation due to higher crosslinking density. This observation supports**the hypothesis that an increase in the alkyne functionality and therefore crosslinking density should reduce degradability**..

When looking at the thiol components of each formulation, BB03 uses a combination of Pentaerythritol Tetrakis(3-Mercaptopropionate) (PETMP), **11,** and 2,2′(Ethylenedioxy)diethanethiol (EDDET), **13**, whereas BB10 used only Dipentaerythritol Hexakis(3-Mercapropriopionate) (DiPETMP), **12**. Compound **13** is known to reduce crosslinking density due to its accessible thioether group (Huang et al. 2022), potentially resulting in more rapid degradation. Since **12** is a hexafunctional thiol, it has a higher alkyne functionality per gram than **11** in BB03. This complexity increases the crosslinking density of BB10, making it more resistant to degradation, aligning with the hypothesis that increased thiol functionality should reduce degradability. Moreover, the potential steric hindrance from **12** might contribute to the slower degradation rate of BB10.

Both BB03 and BB10 contain PTMCPY, **1** which includes carbonate linkages known to undergo hydrolysis in the presence of strong bases to form alcohols and carbonate salts (LibreTexts 2023). BB03 additionally contains IBBC, **4**, another carbonate-based compound, which aligns with the hypothesis that the introduction of more carbonate ester groups should increase degradability. This is reflected in the faster degradation of BB03 (Scheme 1) compared to BB10, which contains 1,7-octadiyne, **10** an alkyne resistant to such hydrolysis due to its hydrocarbon nature (Scheme 2).

BB07 and BB08 both incorporate IPDUB, **7**, which includes urethane groups. In comparison to carbonate esters, esters, acetals and amides, urethane groups are relatively resistant to hydrolysis (Huang et al., 2014). While BB07 and BB08 showed a slightly delayed degradation with significant degradation starting only around 4 h, they still reach complete degradation relatively quickly. This observation only partially supports **the hypothesis that the introduction of more urethane groups should decrease degradability**, suggesting that whilst the urethane might increase toughness via hydrogen bonding which can diminish crack-propagating forces, its effect on degradability might not be as pronounced as expected or could be offset by other formulation components.

BB02 and BB05 both degrade completely by 4 h, suggesting that other components or lower crosslinking densities may play a significant role. In particular, BB02 contains 1,7-octadiyne, **10** (an alkyne resistant to hydrolysis) and yet shows rapid degradation, highlighting the interplay of different constituents and their overall impact on material stability. In general, as long as there were carbonate esters somewhere in

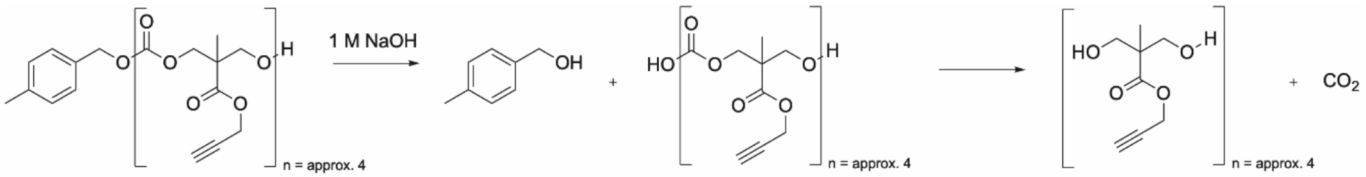

Scheme 1. Possible hydrolysis route for PTMCPY, **1**, present in both BB03 and BB10, in 1 M NaOH, proceeding via a nucleophilic acyl addition–elimination.

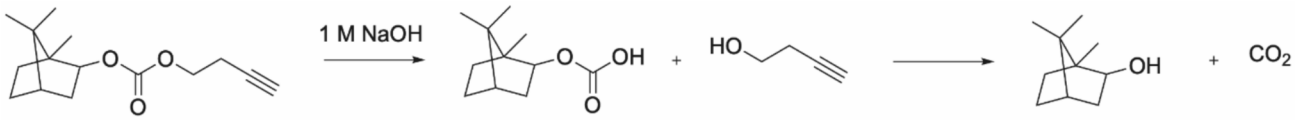

Scheme 2. Possible hydrolysis route for IBBC, **4,** present in BB03, in 1 M NaOH, proceeding via a nucleophilic acyl addition–elimination.

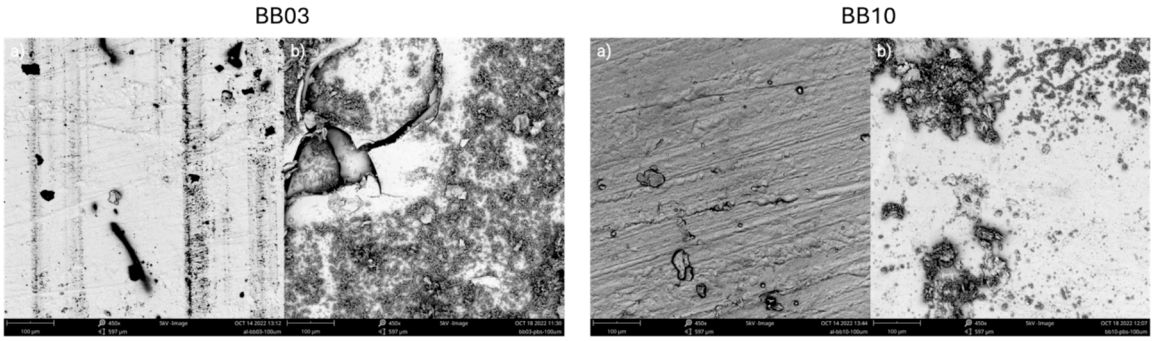

Fig. 12. SEM images of BB03 and BB10 at 450x magnification, 100 μm field of view diameter. Comparison of the sample at a) 0 days and b) after two months of immersion in PBS solution at 37 °C.

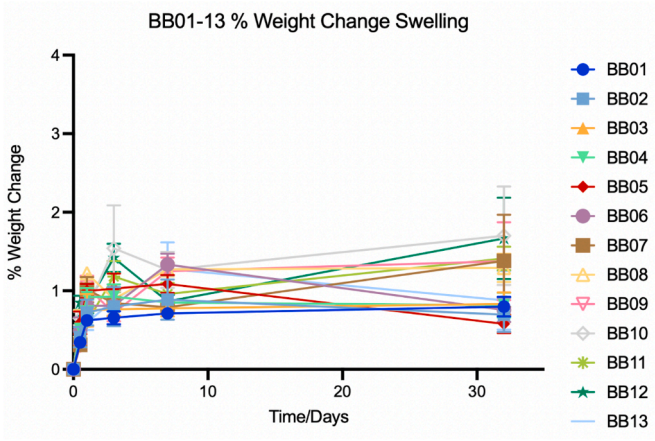

Fig. 13. Swelling studies of samples BB01-13 in dH_2O, showing the % change in mass over a period of 0.5, 1, 3, 7 and 32 d. Each line represents the mean mass of each sample with error bars.

the polymer network, degradation will occur, and hence the number of carbonate ester groups per gram likely plays a less significant factor in relation to degradation factors than hydrophilicity, low crosslinking density, etc.

3.3.2. *Degradation in PBS*

Degradation studies were conducted in PBS over an extended period to provide a more biologically relevant assessment than sodium hydroxide. Initial observations after seven days indicated partial degradation, evident by flaking of the top layer. However, examinations conducted after one year revealed that none of the samples exhibited signs of complete degradation. This slow degradation rate in a biologically relevant medium like PBS shows the complexity of predicting degradation behaviours based solely on chemical composition and highlights the need for long-term studies to fully understand the degradation pathways and rates.

Further insights were gained from scanning electron microscopy (SEM) images that were acquired for all samples at two distinct time intervals: initially and after a period of two months. For instance, BB03, which had shown the most rapid degradation in 1 M NaOH, displayed notable cracking and significant surface erosion after two months in

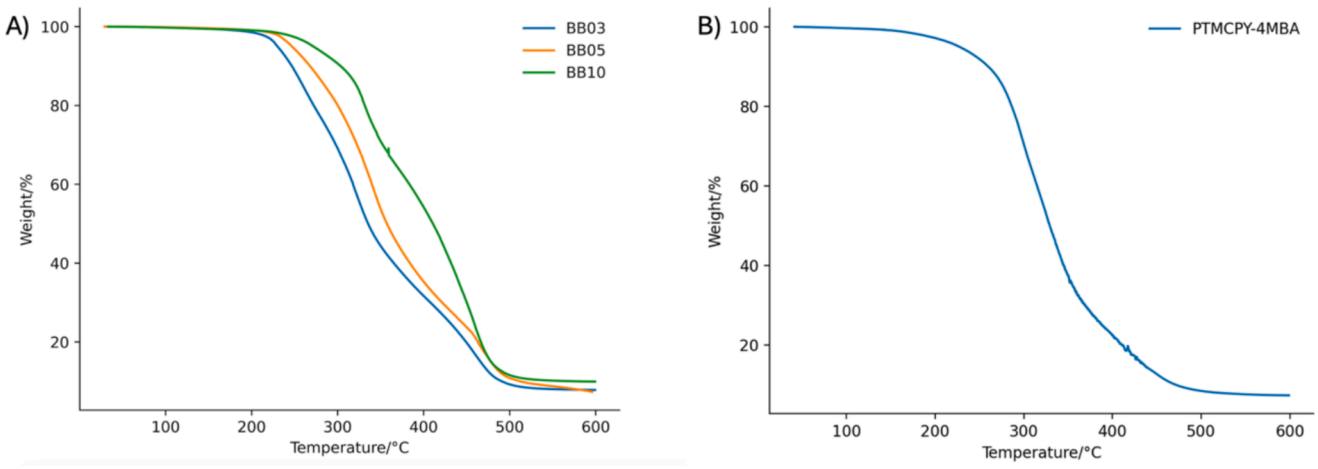

Fig. 14. A) TGA thermogram of BB03, BB05 and BB10. Heating rate 10 °C/min; temperature range 20 to 600 °C; under nitrogen atmosphere. B) TGA thermogram of PTMCPY. Heating rate 10 °C/min; temperature range 20 to 600 °C; under nitrogen atmosphere.

Table 2
Thermal properties of the UV-cured resins. T_o denotes the onset temperature, T_p denotes the maximum thermal degradation temperature, and w_{char} denotes the char yield.

Sample	T_o/ °C	T_p/ °C	w_{char}/%
BB01	296	490	6.6
BB02	270	494	6.9
BB03	224	487	7.8
BB04	221	497	5.2
BB05	237	498	7.3
BB06	282	488	7.2
BB07	291	491	9.8
BB08	277	489	8.0
BB09	306	494	8.8
BB10	249	479	4.8
BB11	311	490	8.0
BB12	276	483	5.4
BB13	310	489	4.3

PBS, highlighting its relative instability even under milder conditions (Fig. 12). In contrast, BB10, which consistently demonstrated slower degradation rates, showed minimal surface erosion over the same period. Despite some evidence of surface degradation, the bulk of the material remained intact, indicating a higher resistance to the hydrolytic conditions within PBS (Fig. 12). SEM images of the remaining BB01-13 formulations are captured in Fig. S11.

3.4. Swelling studies of the mould-cured formulations

Swelling studies were also conducted on all 13 formulations in dH_2O to assess water uptake (Fig. 13). Minimal changes in mass were observed over 32 days for each formulation, in addition to height, width and depth in mm (Figs. S12-S14), indicating that the materials maintain their structural integrity under these conditions. This stability is advantageous for constructs that must perform under the influence of fluids without changing shape unexpectedly.

The composition of these formulations, including PTMCPY, **1** and various thiol and alkyne compounds, suggests a high degree of crosslinking. This high crosslink density likely prevents excessive water uptake, maintaining mechanical integrity and performance. This is useful for biomedical applications, and for applications needing materials that retain their shape in moist conditions without sacrificing functional integrity e.g. tissue engineering and bone scaffolds (Asmussen and Peutzfeldt, 2001; Wu et al., 2022).

3.5. Thermal analysis

Thermal analysis techniques were used to characterise the thermal stability and thermal transitions of the mould-cured resins. Thermogravimetric analysis (TGA) provides insights into the thermal degradation behavior, and differential scanning calorimetry (DSC) complements this by evaluating thermal transitions, such as the T_g which is critical for understanding the mechanical properties, processability, and potential applications of the materials, such as shape memory polymers.

3.5.1. Thermogravimetric analysis of the mould-cured formulations

TGA thermograms of all UV-cured resins were run, and those with fastest degradation in 1 M NaOH (BB03), shape memory properties (BB05), and slowest degradation in 1 M NaOH (BB10) are presented in Fig. 14**a**. TGA thermograms for the remaining BB01-BB13 formulations and the oligomers present in the formulations can be found in Figs. S15 and S16. The degradation process of BB01-13 can be divided into four stages (Table 2) (Hu et al. 2019). The first stage (<240 °C) was slowest, which is due to the removal of residual low molecular-weight volatiles such as water, solvents and unreacted monomers (Liu et al. 2016). The second stage at 240–350 °C can be assigned to the decomposition of PTMCPY, **1**, since the % weight loss of the sample corresponds to the % w/w in the corresponding formulation, and the TGA of PTMCPY (Fig. 14**b**) indicates that approx. 80 % of weight loss observed occurred within this temperature range. The third stage at 350–500 °C was quickest and can be designated to the degradation of the cross-linked bonds and char formation, while the last stage (>500 °C) corresponded to the gradual degradation of char residue which varied between 4.3–9.8 % of the original sample mass.

When the content of PTMCPY, **1**, decreased from 34 % (BB03) and 31 % (BB05) to 20 % for BB10, the onset degradation temperature (T_o) increased slightly from 224 °C for BB03 and 237 °C for BB05 to 249 °C for BB10. The maximum thermal degradation temperature (T_p) increased slightly from 479 °C for BB10 to 487 °C for BB03 and 498 °C for BB05, and the char yield (w_{char}) decreased from 7.8 % for BB03 to 7.3 % for BB05 and 4.8 % for BB10. These observations indicate that the differences in the formulation between BB03, BB05 and BB10 did not influence the thermal stability of the resins too much. In BB10, the use of the alkyne 1,7-octadiyne, **10** instead of a carbonate as used for BB03 and BB05, and a greater % of the thiol component (69 % DiPETMP, **12**, compared to 43 % and 47 % of PETMP, **11** used in BB03 and BB05 respectively) meant that the third stage made up a larger proportion of the overall % weight loss for BB10. The main difference in the formulation between BB03 and BB05 was the use of different carbonates (IBBC, **4** for BB03 and 1,6-hexanedibutynyl carbonate (HDBC) for BB05) in the formulation, however it seems as though this did not influence the thermal stability of these two resins too much.

Table 3
Glass transition temperature (T_g) values for formulations BB01-13 via different DSC heating methods. A heating ramp of 10 °C/min, 100 °C/min, and sequential heat-cool-heat cycles at 10 °C/min were used. The T_g values recorded during the initial and subsequent heating phases highlight the influence of heating rate and thermal history on the T_g of the polymers.

DSC Heating Cycle	10 °C/min ramp	100 °C/min ramp	10 °C/min Heat-Cool-Heat: 1st heating cycle	10 °C/min Heat-Cool-Heat: 2nd heating cycle
BB01	13.1	31.6	7.9	13.3
BB02	4.6	15.1	5.2	10.5
BB03	2.6	17.0	5.0	9.1
BB04	5.6	21.4	5.0	7.0
BB05	−1.2	13.1	−1.2	3.2
BB06	6.3	17.7	8.0	10.0
BB07	12.5	24.8	13.4	19.4
BB08	16.5	30.0	15.1	22.7
BB09	17.6	36.6	17.1	22.9
BB10	23.3	36.2	26.6	33.9
BB11	11.2	23.2	8.5	15.1
BB12	5.1	21.7	7.9	11.5
BB13	8.0	23.2	8.4	12.8

3.5.2. Differential scanning calorimetry of the mould-cured formulations

Differential scanning calorimetry was used to examine how the different formulations influenced the thermal properties of the materials. The primary focus was on determining the T_g for each formulation, which indicates whether a material exists as a rigid, glassy structure or as a flexible, rubbery system at room temperature, offering insights into a materials mechanical properties. It can also help identify their suitability as shape memory polymers (SMPs) for future work.

The characterisation of photoreactive formulations via differential scanning calorimetry (DSC) involved two heating rates: a standard 10 °C/min and 100 °C/min. This separated approach was used to differentiate thermodynamic from kinetic events within the samples. Complete thermograms for all formulations across the 10 °C/min and 100 °C/min ramps are provided in Figs. S17 and S18. While kinetic events such as crystallization temperature (T_c) and glass transition temperature (T_g) are rate-dependent, the measured melting temperature (T_m) **is less affected by heating rate (it can also be influenced by the heating rate due to factors such as superheating effects and thermal**

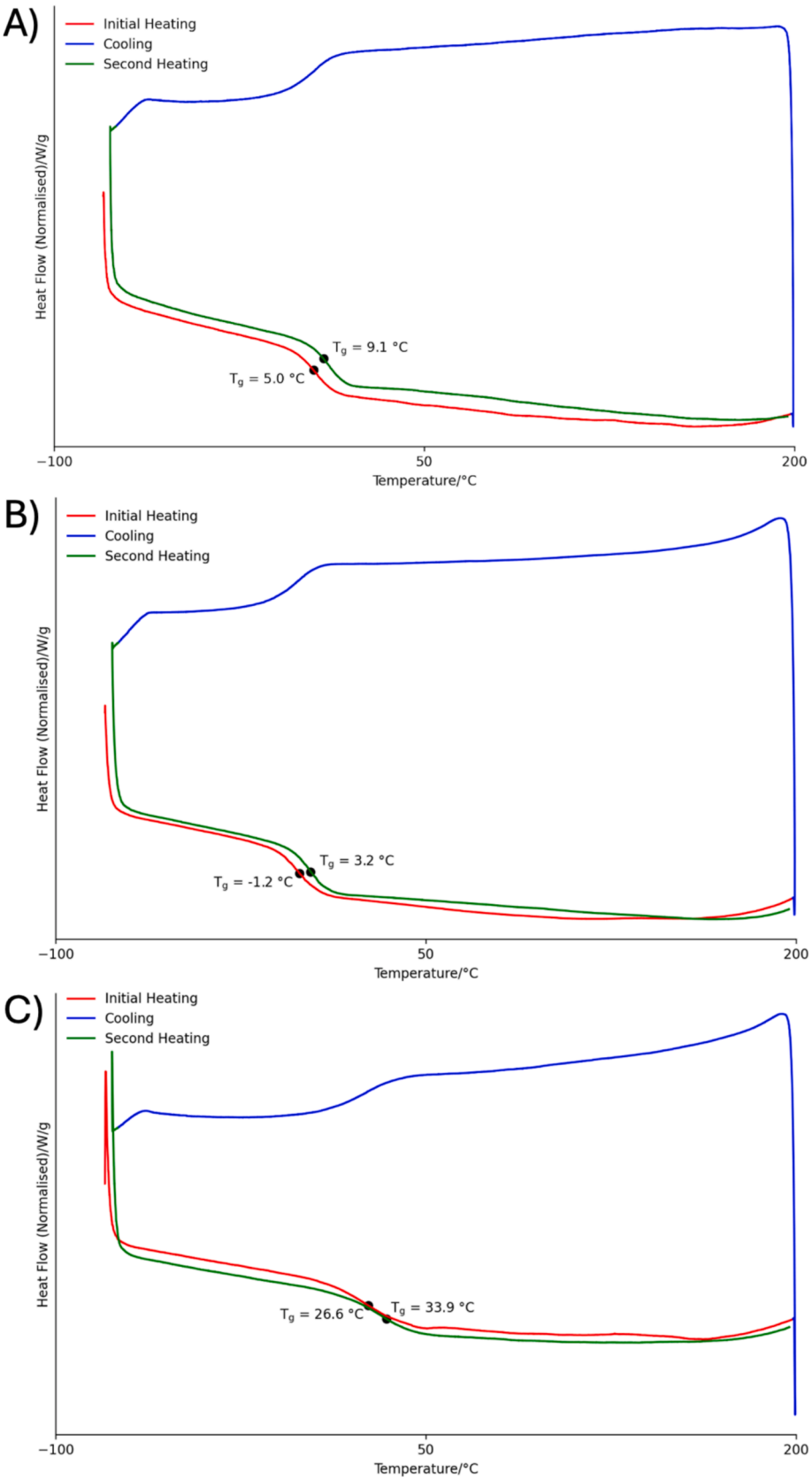

Fig. 15. DSC profile of A) BB03, B) BB05, C) BB10, showing Heat Flow over a heat-cool-heat cycle where the samples were ramped 10 °C/min from −80 °C to 200 °C, down to −80 °C at 10 °C/min and back up to 200 °C at 10 °C/min.

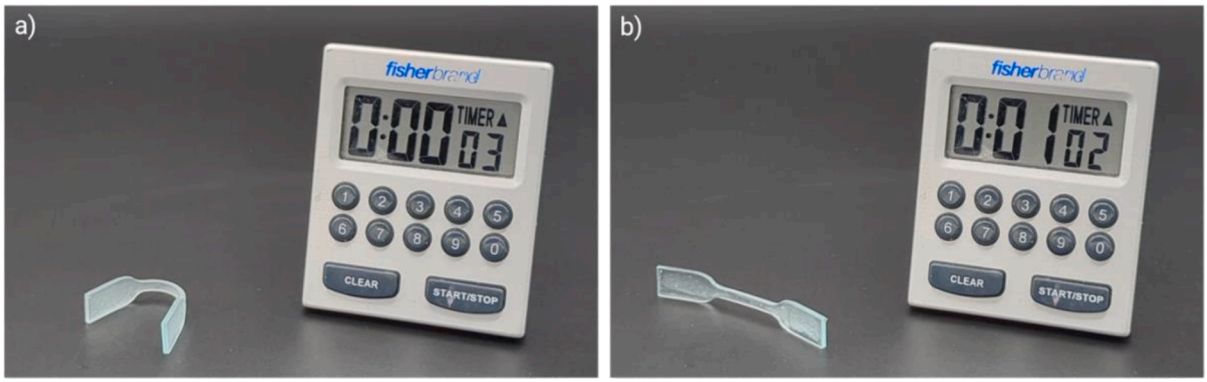

Fig. 16. Pictures from a time-lapse recording at a) 0 s and b) 1 min, capturing the recovery of BB05 from a deformed shape to its original shape upon warming to room temperature, validating its shape memory properties at sub-zero temperatures.

lag). Additionally, the presence of primary thermodynamic transitions is material-dependent, and their relevance should be carefully considered in context. For example, the consistent increase in T_g for samples when the heating rate is increased from 10 °C/min to 100 °C/min e.g. from 2.6 to 17.0 °C for BB03 helped to identify that this transition was a T_g.

A further heat-cool-heat cycle was run across all formulations and oligomers PTMCPY and IPDUT, showing a consistent rise in T_g values between the first and second heating cycles (Table 3, Fig. 15, Figs. S19-S20). This observation suggested that the thermal history of the polymers played a role in their thermal response upon reheating, a factor that could influence their shape memory characteristics.

As shown in Table 3, all materials display a glass transition temperature below room temperature besides BB10 hence explaining their rubbery elastic properties at room temperature, besides BB10 which is rigid and brittle at room temperature. This is attributed to the use of "hard" DiPETMP, **12** as its thiol segment in the formulation, as mentioned previously since it is a hexafunctional thiol, this complexity increases the crosslinking density of BB10, ultimately giving it increased rigidity and increased T_g.

BB05 exhibited a negative T_g at the standard heating rate, showing a potential for shape memory behaviour at sub-zero temperatures. This led to a shape memory assessment, where BB05 was mould-cured and frozen overnight in a deformed shape (Fig. 16).

The lower T_g of formulations BB01 to BB13, ranging from −1.2 to 23.3 °C, demonstrate advantages over traditional higher T_g methacrylate-based polymers (e.g. polymethyl methacrylate (PMMA) has a T_g typically around 105 °C). T_g values near or below physiological temperatures confer enhanced biocompatibility and comfort. This is attributed to their inherent flexibility and toughness, important for ensuring conformability to biological tissues and minimising discomfort or irritation in implantable drug delivery systems. Toughness will also lower the risk of device failure *in situ*, which would otherwise require the removal of the device and failure of treatment. This mechanical compliance also potentially lowers the foreign body response, crucial for long-term implant viability. The lower T_g of these formulations facilitates improved processing at reduced temperatures, which is an important factor in encapsulating temperature-sensitive therapeutic agents. This is beneficial for maintaining the integrity and efficacy of delicate drugs like proteins or RNA-based therapies, which may degrade or lose functionality under higher processing temperatures.

4. Conclusions

This research illustrates the potential of fully degradable 3D printed DLP formulations for developing future biodegradable implants, with further work required to evaluate their suitability for drug delivery applications. The findings show that the properties of thiol-ene and thiol-yne systems can be modified to create formulations (BB01 to BB13) with tailored mechanical properties such as tensile strength, elongation at break, glass transition temperature and precisely controlled degradation rates. These characteristics are essential for implants that need to withstand the physiological environment while providing targeted therapeutic action without the need for surgical removal after treatment. BB10 showed high stiffness suitable for structural applications within the body, while BB03 exemplified rapid degradability which is a desirable trait for temporary implants that dissolve after fulfilling their therapeutic purpose, thereby avoiding the complications associated with permanent implants. The full degradability of these materials not only show potential to enhance patient safety and comfort but also align with a need for more effective and less invasive treatments highlighted at the outset of the study. By combining 3D printing with fully degradable polymers, this shows promise for more effective and personalised therapeutic solutions.

Further research is focusing on refining these formulations to achieve precise degradation rates and mechanical properties tailored for specific therapeutic applications, such as sustained drug release or temporary scaffolds for tissue repair. This includes conducting *in vivo* studies to validate their long-term biocompatibility, and optimising their suitability for drug delivery systems. Additionally, the degradation products are being evaluated to assess both their toxicity and risk of bioaccumulation, ensuring that breakdown products degrade into sufficiently small, non-toxic fragments to mitigate risks such as microplastic formation and bioaccumulation.

CRediT authorship contribution statement

A. Locks: Writing – review & editing, Writing – original draft, Methodology, Investigation, Formal analysis, Data curation. **B.J. Bowles:** Writing – review & editing, Writing – original draft, Methodology, Investigation, Formal analysis, Data curation, Conceptualization. **S. Brown:** Writing – review & editing, Supervision, Resources, Methodology, Investigation, Funding acquisition. **H.C. Hailes:** Writing – review & editing, Supervision. **S.T. Hilton:** Writing – review & editing, Writing – original draft, Supervision, Resources, Project administration, Funding acquisition, Conceptualization.

Declaration of competing interest

The authors declare the following financial interests/personal relationships which may be considered as potential competing interests: [Stephen Hilton reports financial support was provided by Scott Bader Co Ltd. Helen Hailes, Stephen Hilton and Amy Locks reports financial support was provided by EPSRC. Stephen Hilton reports a relationship with 3D Synthesis Ltd that includes: board membership and equity or stocks. If there are other authors, they declare that they have no known

competing financial interests or personal relationships that could have appeared to influence the work reported in this paper].

Acknowledgements

This work was kindly funded by University College London and the Engineering and Physical Sciences Research Council (EPSRC) through the award of PhD studentship to Amy Locks in the Centre for Doctoral Training in Transformative Pharmaceutical Technologies under Grant EP/S023054/1 and Scott Bader via a postdoctoral fellowship for Dr Benjamin J. Bowles. Additional thanks to Scott Bader for performing the GPC analyses, and to the National Mass Spectrometry Facility at Swansea University for performing the MALDI-TOF MS analyses, as detailed in the Supporting Information. Tom Locks for his assistance in developing the initial coding required to generate some of the figures presented in this article. The funding sources had no role in the study design, analysis, interpretation of data, writing of the manuscript nor in the decision to submit the article for publication.

Appendix A. Supplementary data

Supplementary data to this article can be found online at https://doi.org/10.1016/j.ijpharm.2025.125432.

Data availability

Data will be made available on request.

Reference

Albelasy, E., Hamama, H., Chew, H., Montasser, M., Mahmoud, S., 2024. J. Esthet. Restor. Dent. 36, 723–736. https://doi.org/10.1111/jerd.13193.
Asmussen, E., Peutzfeldt, A., 2001. *Eur. J. Oral Sci.* 109, 282–285. https://doi.org/10.1034/j.1600-0722.2001.00057.x.
Balakrishnan, B., Jayakrishnan, A., 2005. Biomaterials. 26, 3941–3951. https://doi.org/10.1016/j.biomaterials.2004.10.005.
Bulanova, E.A., 2017. Biofabrication 93, 1–28. https://doi.org/10.1088/1758-5090/aa7fdd.
Chew, S.A., Danti, S., 2017. Adv. Healthc. Mater. 6. https://doi.org/10.1002/adhm.201600766.
Esfandiari, P., Ligon, S.C., Lagref, J.J., Frantz, R., Cherkaoui, Z., Liska, R., 2013. Polym. Chem. 51, 4261–4266. https://doi.org/10.1002/pola.26848.
Exner, A.A., Saidel, G.M., 2008. Expert Opin. Drug Deliv. 5, 775–788. https://doi.org/10.1517/17425247.5.7.775.
Gao, J., Qian, F., Szymanski-Exner, A., Stowe, N., Haaga, J., 2002. J. Biomed. Mater. Res. 62, 308–314. https://doi.org/10.1002/jbm.10292.
Goyanes, A., Martinez, P.R., Buanz, A., Basit, A.W., Gaisford, S., 2015. Int. J. Pharm. 494, 657–663. https://doi.org/10.1016/j.ijpharm.2015.04.069.
Heller, C., Schwentenwein, M., Russmüller, G., Koch, T., Moser, D., Schopper, C., Varga, F., Stampfl, J., Liska, R.J., 2010. Polym. Sci. Part A Polym. Chem. 49. https://doi.org/10.1002/pola.24476.
Hoyle, C.E., Lee, T.Y., Roper, T.J., 2004. Polym. Sci. Part A Polym. Chem. 42, 5301–5338. https://doi.org/10.1002/pola.20366.
Hu, Y., Shang, Q., Bo, C., Jia, P., Feng, G., Zhang, F., Liu, C., Zhou, Y., 2019. ACS Omega 4, 12505–12511. https://doi.org/10.1021/acsomega.9b01174.
Huang, Y., Cao, B., Xu, C., Fan, Q., Shao, J., 2014. Text. Res. J. 85, 759–767. https://doi.org/10.1177/0040517514551467.
Huang, J., Fu, P., Li, W., Xiao, L., Chen, J., Nie, X., 2022. RSC Adv. 12, 23048–23056. https://doi.org/10.1039/D2RA04206A.
B. Husár S.C. Ligon H. Wutzel H. Hoffmann R. Liska Prog. Org. Coat. 77 2014 1789 1798 10.1016/j.porgcoat.2014.06.005.
Husar, B., Liska, R., 2012. Chem Soc. Rev. 41, 2395–2405. https://doi.org/10.1039/C1CS15232G.
Hutmacher, D.W., Sittinger, M., Risbud, M.V., 2004. Trends Biotechnol. 22, 354–362. https://doi.org/10.1016/j.tibtech.2004.05.005.
Jain, R.A., 2000. Biomaterials. 21, 2475–2490.
Kim, H., Jeon, H., Shin, G., Lee, M., Jegal, J., Hwang, S.Y., Oh, D.X., Koo, J.M., Eom, Y., Park, J., 2021. Green Chem. 23, 2293–2299. https://doi.org/10.1039/D0GC04072J.
Krukiewicz, K., Zak, J.K., 2016. Mater. Sci. Eng. C. 62, 927–942. https://doi.org/10.1016/j.msec.2016.01.063.
Leong, K.F., Cheah, C.M., Chua, C.K., 2003. Biomaterials. 24, 2363–2378. https://doi.org/10.1016/S0142-9612(03)00030-9.
Liaw, C.-Y., Guvendiren, M., 2017. Biofabrication. 9. https://doi.org/10.1088/1758-5090/aa7279.
LibreTexts. Hydrolysis of Esters. Available at: https://chem.libretexts.org/Courses/Eastern_Mennonite_University/EMU%3A_Chemi stry_for_the_Life_Sciences_(Cessna)/15%3A_Organic_Acids_and_Bases_and_Som e_of_Their_Derivatives/15.09_Hydrolysis_of_Esters (accessed May 1, 2024).
Ligon, S.C., Liska, R., Stampfl, J., Gurr, M., Mülhaupt, R., 2017. Chem Rev. 117, 10212–10290. https://doi.org/10.1021/acs.chemrev.7b00074.
Liu, J., Liu, R., Zhang, X., Tang, H., Liu, X., 2016. Prog. Org. Coat. 90, 126–131. https://doi.org/10.1016/j.porgcoat.2015.10.012.
Melchels, F.P.W., Feijen, J., Grijpma, D.W., 2010. Biomaterials 31, 6121–6130. https://doi.org/10.1016/j.biomaterials.2010.04.050.
Naira, D.P., Cramer, N.B., Scott, T.F., Bowman, C.N., Shandas, R., 2010. Polymer. 51, 4383–4389. https://doi.org/10.1016/j.polymer.2010.07.027.
Norman, J., Madurawe, R.D., Moore, C.M.V., Khan, M.A., Khairuzzaman, A., 2017. Adv. Drug Deliv. Rev. 108, 39–50. https://doi.org/10.1016/j.addr.2016.03.001.
Nyga, A., Cheema, U., Loizidou, M.J., 2011. Cell Commun Signal. 5, 239–248. https://doi.org/10.1007/s12079-011-0132-4.
Oesterreicher, A., Gorsche, C., Ayalur-Karunakaran, S., Moser, A., Edler, M., Pinter, G., Schlogl, S., Liska, R., Griesser, T., 2016. Macromol. Rapid Commun. 37, 1701–1706. https://doi.org/10.1002/marc.201600369.
Oesterreicher, A., Ayalur-Karunakaran, S., Moser, A., Mostegel, F.H., Edler, M., Kaschnitz, P., Pinter, G., Trimmel, G., Schlogl, S., Griesser, T., 2016. J. Polym. Sci., Part A: Polym. Chem. 54, 3484–3494. https://doi.org/10.1002/pola.28239.
Oesterreicher, A., Moser, A., Edler, M., Griesser, H., Schlögl, S., Pichelmayer, M., Griesser, T., 2017. Macromol. Mater. Eng. 302. https://doi.org/10.1002/mame.201600450.
Olofsson, K., Granskog, V., Cai, Y., Hult, A., Malkoch, M., 2016. RSC Adv. 6, 2639826405. https://doi.org/10.1039/C5RA23142F.
Palo, M., Holländer, J., Suominen, J., Yliruusi, J., Sandler, N., 2017. Expert Rev. Med. Devices. 14, 685–696. https://doi.org/10.1080/17434440.2017.1363647.
Pezzana, L., Wolff, R., Melilli, G., Guigo, N., Sbirrazzuoli, N., Stampfl, J., Liska, R., Sangermano, M., 2022. Polym. 254. https://doi.org/10.1016/j.polymer.2022.125097.
Plastics - The Facts; 2022. Available online: https://plasticseurope.org/knowledgehttps://plasticseurope.org/knowledge-hub/plastics-the-facts-2022/hub/plastics-the-facts-2022/ (accessed May 1, 2024).
Prasad, L.K., Smyth, H., 2015. Drug Dev. Ind. Pharm. 42, 1019–1031.
Revilla-León, M., Meyers, M.J., Zandinejad, A., Özcan, M., 2019. J. Esthet. Restor. Dent. 31, 51–57. https://doi.org/10.1111/jerd.12438.
Roppolo, I., Frascella, F., Gastaldi, M., Castellino, M., Ciubini, B., Barolo, C., Scaltrito, L., Nicosia, C., Zanetti, M., Chiappone, A., 2019. Polym. Chem. 10, 5950–5958. https://doi.org/10.1039/c9py00962k.
Stephens, F.O., Aigner, K.R., 2009. *Basics of Oncology*. Springer, Berlin.
Tan, E.W.P., Hedrick, J.L., Arrechea, P.L., Erdmann, T., Kiyek, V., Lottier, S., Yang, Y.Y., Park, N.H., 2021. Macromolecules 54, 1767–1774. https://doi.org/10.1021/acs.macromol.0c02880.
von Burkersroda, F., Schedl, L., Gopferich, A., 2002. Biomaterials. 23, 4221–4231. https://doi.org/10.1016/S0142-9612(02)00170-9.
Wang, J., Jiang, A., Joshi, M., Christoforidis, J., 2013. Mediators Inflamm. 8. https://doi.org/10.1155/2013/780634.
Wang, Z., Lu, Q., Li, X., Zhou, Y., Xiao, Y., Lang, M., 2023. Eur. Polm. J. 202, 112586. https://doi.org/10.1016/j.eurpolymj.2023.112586.
Wolinsky, J., Colson, Y., Grinstaff, M.J., 2012. J. Control. Release. 159, 1–34. https://doi.org/10.1016/j.jconrel.2011.11.031.
Wu, Y., Simpson, M.C., Jin, J., 2021. Macromol. Chem. Phys. 222. https://doi.org/10.1002/macp.202000435.
Wu, Y., Simpson, M.C., Jin, J., 2022. *C*hemistrySelect. 7. https://doi.org/10.1002/slct.202200319.
Yeong, W.-Y., Chua, C.-K., Leong, K.-F., Chandrasekaran, M., 2004. Trends Biotechnol. 22, 643–652. https://doi.org/10.1016/j.tibtech.2004.10.004.
Zhang, J., Xiao, P., 2018. Polym. Chem. 9, 1530–1540. https://doi.org/10.1039/C8PY00157J.

Glossary

3D Printing: Manufacturing process that builds three-dimensional objects from a digital model by layering material.
Alkyne: Organic compounds containing a carbon–carbon triple bond.
Biocompatibility: The capability of a material to perform with an appropriate host response when used within a biological environment.
Biodegradability: The ability of materials to break down into simpler, non-toxic substances through biological activity.
Cross-linking: Chemical linking of two or more molecules by covalent bonds within a polymer, enhancing material properties like stability and elasticity.
Degradation: The process where material properties deteriorate over time due to environmental conditions, chemical reactions, or biological activity.
Ester Linkage Hydrolysis: Chemical reaction where ester bonds are split into acids and alcohols by water.
Hydrolysis: A chemical breakdown process involving the reaction of water with another substance.
Mechanical Properties: Characteristics that describe how a material responds to mechanical stresses, including elasticity, tensile strength, and hardness.
Oligomer: A molecule that consists of a few monomer units.
Photopolymerisation: Process by which light energy initiates the polymerisation of monomers into polymers.
Photoreactivity: The characteristic of a material to undergo chemical change upon exposure to light.
Polymerisation: The process of reacting monomer molecules together in a chemical reaction

to form polymer chains.

Shape Memory: The property of a material to return to its original shape after deformation when exposed to a specific stimulus, such as heat.

Step-Growth Polymerisation: A type of polymerisation in which bi-functional or multi-functional monomers link in sequences to form high molecular weight polymers.

Thermal Behaviour: The response of materials to changes in temperature, such as thermal expansion, contraction, melting, or decomposition.

Thiol: An organic compound containing a sulphur-hydrogen group, −SH.

Thiol-Ene Polymerisation: A polymerisation process involving a step-growth reaction between a thiol group and an alkene, forming a thioether linkage.

Thiol-Yne Polymerisation: A polymerisation process involving a step-growth reaction between a thiol group and an alkyne, forming a thioether linkage. This process typically results in the creation of a highly cross-linked polymer network.

Viscosity: A fluid's measure of resistance to gradual deformation by shear stress or tensile stress.